ADVANCED MATERIALS
www.advmat.de

High-Performance Polymer Tandem Solar Cells Employing a New n-Type Conjugated Polymer as an Interconnecting Layer

Kai Zhang, Ke Gao, Ruoxi Xia, Zhihong Wu, Chen Sun, Jiamin Cao, Liu Qian, Weiqi Li, Shiyuan Liu, Fei Huang, Xiaobin Peng,* Liming Ding,* Hin-Lap Yip,* and Yong Cao*

Organic solar cells (OSCs) offers several distinct advantages such as light weight, good mechanical flexibility, and low costs over other photovoltaic technologies, making them a potential future renewable energy source.[1–3] While over the past decade the performance of OSCs continued to improve with power conversion efficiency (PCE) now reaching over 10% for single-junction cells,[4,5] further breakthrough on the PCE is required in order to achieve broader applications. To achieve the performance goal, advances in the development of more efficient light-harvesting and interface materials are required.[6–9] In addition, tandem configuration is another promising approach to improve the OSC performance by tackling the main losses in single-junction OSCs, such as narrow absorption window and thermalization losses.[10–13]

Typically, a tandem solar cell consists of a front cell with wide bandgap light harvesting layer and a back cell with narrow bandgap light harvesting layer connected by an interconnecting layer (ICL), which also acts as the recombination center between the two sub-cells. Compared with single-junction device, the tandem one can more efficiently utilize both high energy photons and low energy photons, and also reduce the overall thermalization loss by absorbing the high energy photons in the wide bandgap cell. According to model calculations, maximum PCEs of up to 15% are feasible for double-junction tandem OSCs with an optimized pair of absorber materials with different bandgap energies and complementary absorption spectra.[14,15] In addition to the selection of novel pair of absorbers in different sub-cells, the choice of interfacial materials for constructing the ICL is also very critical for making high-performance tandem OSCs. The ICL typically is composed of a hole-transport-layer (HTL) and electron-transport-layer (ETL) pair at which a quasi-Ohmic-contact should be formed at the junction for efficient bipolar recombination. Sometimes a thin metal film or metal nanoparticle is introduced at the HTL/ETL interface to further improve the recombination efficiency.[16–18] Another important criterion for the selection of the HTL/ETL ICL is its compatibility for building multilayer cells from solution processes. The HTL and ETL should be processed from orthogonal solvents and be able to provide good solvent resistance for the bottom sub-cell to prevent erosion of under layers.[11,19]

The most popular ICL structures reported are p-type metal oxide combined with organic material, such as MoO_3/PFN,[16,20] or p-type polymer combined with metal oxide, such as PEDOT:PSS/ZnO,[21–25] in the case of inverted-type tandem OSCs. For conventional tandem OSCs, the ICL structure is composed of a n-type metal oxide combined with p-type polymer, such as ZnO/PEDOT:PSS[26] and TiO_x/PEDOT:PSS,[11,27,28] or n-type metal oxide combined with p-type metal oxides, such as ZnO/MoO_3.[29,30] Although these combinations often result in excellent device performance, the inorganic metal oxides may suffer from their intrinsic brittleness and may not be fully compatible with flexible or wearable application of OSCs. In addition, in some cases the n-type metal oxides degrade by reacting with the acidic PEDOT:PSS and reduce the device stability.[31] Therefore, there are increasing efforts focused on the development of organic/organic based ICLs, such as PEDOT:PSS/polyelectrolyte. Amine-containing water/alcohol-soluble polymers and polyelectrolytes were proven to be efficient ETL for OPVs, which can modify the work function of electrode by forming favorable interfacial dipole to improve electron extraction property.[32,33] Kippelen and co-workers successfully reported the use of PEDOT:PSS/PEIE ICL to construct inverted tandem OSCs and later on similar device configuration was verified by Jang and co-workers.[34,35] In the case of conventional tandem OSCs, Yang and co-workers adopted a relatively complicated polyelectrolyte 1/polyelectrolyte 2/PEDOT:PSS trilayer structure in order to optimize the recombination property at the ICL.[36] Ideally, simplified ETL/HTL ICL structure could also be realized

Dr. K. Zhang, K. Gao, R. Xia, Z. Wu, C. Sun,
Prof. F. Huang, Prof. X. Peng,
Prof. H.-L. Yip, Prof. Y. Cao
Institute of Polymer Optoelectronic
Materials and Devices
State Key Laboratory of Luminescent
Materials and Devices
South China University of Technology
Guangzhou 510640, P. R. China
E-mail: msfhuang@scut.edu.cn; chxbpeng@scut.edu.cn;
msangusyip@scut.edu.cn

Dr. J. Cao, L. Qian, Prof. L. Ding
National Center for Nanoscience and Technology
Beijing 100190, P. R. China
E-mail: ding@nanoctr.cn

W. Li, Prof. S. Liu
State Key Laboratory of Digital Manufacturing
Equipment and Technology
Huazhong University of Science and Technology
Wuhan, Hubei 430074, P. R. China

Prof. S. Liu
Wuhan Eoptics Technology Co. Ltd.
Wuhan, Hubei 430075, P. R. China

DOI: 10.1002/adma.201506270

in the conventional-type tandem OSCs by developing more efficient polymer-based ETL.

Herein, we employed a newly developed amine-containing conjugated polymer PF3N-2TNDI[37,38] as the ETL and PEDOT:PSS as the HTL to construct the ICL for conventional tandem OSCs. A 2 nm Ag film was deposited to further improve the recombination property at the ETL/HTL interface. A wide bandgap PThBDTP:$PC_{71}BM$[39] sub-cell (sub-cell 1) and a narrow bandgap DPPEZnP-TEH:$PC_{61}BM$[40] sub-cell (sub-cell 2) were chosen to construct the tandem OSC as they show complementary absorption and also both of them can produce single-junction cells with high efficiency. The tandem OSC structure is ITO/PEDOT:PSS/sub-cell 1/PF3N-2TNDI/Ag(2 nm)/PEDOT:PSS/sub-cell 2/PF3N-2TNDI/Ag. The newly designed ICL successfully protected the front cell from being eroded by the solutions used to process the back cell and also provided efficient recombination effect. Optical modeling was applied to provide guideline for the optimization of the thickness of each layer in the tandem cells in order to obtain balanced and maximized photocurrent from the different sub-cells. Finally, high-performance tandem OSCs with PCEs high up to 11.35% and 11.94% were achieved under illumination at 100 and 50 mW cm^{-2}, respectively, which increases about 30% in efficiency when compared to the individual single-junction sub-cells. As all the processes employed to fabricate the tandem OSC were conducted at low temperatures, we took one step further to fabricate the devices on plastic substrate and successfully demonstrated flexible tandem OSCs with PCE over 10%.

The tandem OSC device structure and the chemical structures of the light harvesting materials and the newly developed PF3N-2TNDI ETL are shown in **Figure 1**a,b. The absorption spectra and extinction coefficients (k) of the front-cell active layer PThBDTP:$PC_{71}BM$ and the back-cell active layer DPPEZnP-TEH:$PC_{61}BM$ are shown in Figure 1c,d, respectively. These material combinations were selected because they represent the state-of-the-art bulk heterojunction (BHJ) systems that absorb light in the visible and infrared regions. The main absorption range of PThBDTP:$PC_{71}BM$ (1:1.2, w/w) covers from 300 to 667 nm; the optical bandgap of PThBDTP is 1.86 eV, which was calculated from the thin film absorption onset at 667 nm. The absorption spectrum of DPPEZnP-TEH:$PC_{61}BM$ (1:1.2, w/w) covers a broad range from 300 to 900 nm; the calculated optical bandgap of DPPEZnP-TEH is 1.37 eV. Although there was an overlap between the absorption spectra

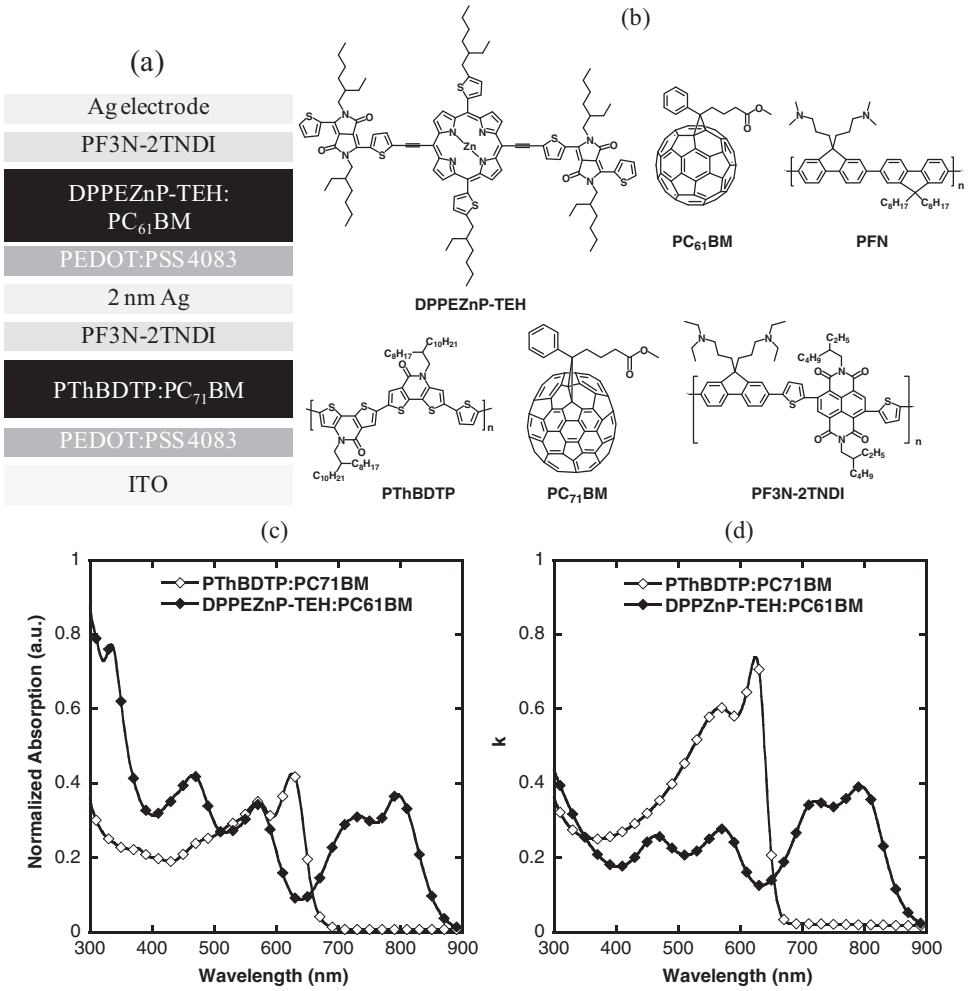

Figure 1. a) Tandem OSC device structure and b) chemical structures of the light harvesting materials and interlayer materials used in this study. c) Absorption spectra and d) extinction coefficient of the active layers for the front and back cells.

of the front and back cells within the range of 300–650 nm, the extinction coefficient of PThBDT:PC_{71}BM at that range is much larger than that of the DPPEZnP-TEH:PC_{61}BM and therefore most of the visible light is expected to be absorbed by the front cell while the narrow bandgap back cell can also help to harvest small portion of the visible light escaped from the front cell. On the other hand, the thermalization loss can be suppressed by taking the advantages of using a wide-bandgap and a narrow-bandgap active layer in the tandem OSCs and the photocurrent mismatch between the sub-cells can be minimized by varying the thickness of the active layer in the front cell and back cell.

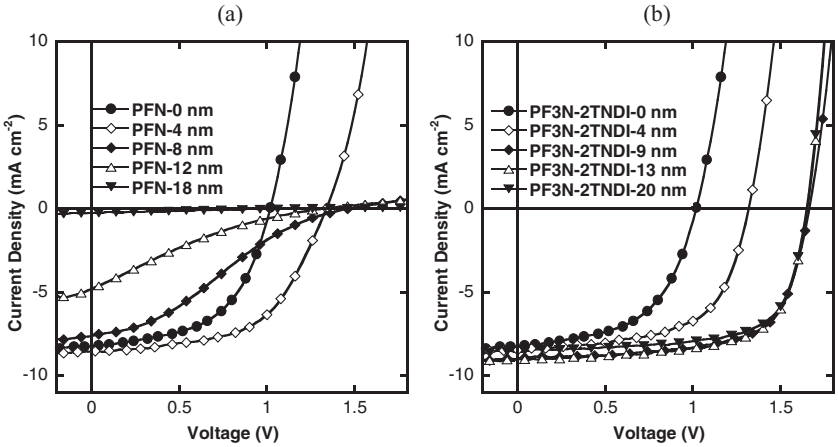

Figure 2. *J–V* characteristics of conventional-type tandem OSCs employing ICL constructed with different thickness of a) PFN and b) PF3N-2TNDI.

Before the construction of tandem OSCs, single-junction sub-cells with device structure of ITO/PEDOT:PSS/BHJ/PF3N-2TNDI/Ag were tested (data summarized in Figure S1 and Table S1 of Supporting Information). For the front cell, a PCE of 8.86% with J_{sc} of 12.6 mA cm^{-2}, V_{oc} of 0.95 V, and fill factor (FF) of 74% was achieved, while for the back cell, a PCE of 8.09% with J_{sc} of 17.01 mA cm^{-2}, V_{oc} of 0.78 V, and FF of 61% was achieved based on the fabrication procedure in previous report.[40] Despite the fact that both cells show high PCEs, the FF obtained in the back cell is obviously lower, which may lead to poor tandem cell efficiency.[41] Therefore, we further optimized the back-cell performance by employing solvent vapor annealing (SVA) treatment, which is a simple and effective way for improving the absorption, morphology, and charge mobility in small molecule-based BHJ.[42] The SVA process was conducted by putting the DPPEZnP-TEH:PC_{61}BM film in a chloroform-vapor-containing Petri dish for different times. We found that with a SVA time of 30 s, there was a significant improvement in device performance with PCE increasing from 8.09% to 8.73% with a J_{sc} of 17.32 mA cm^{-2}, V_{oc} of 0.72 V, and FF of 70%. The SVA was thus proved to be an effective way of enhancing the back-cell performance and can be applied to the fabrication of the tandem solar cell. It is also worth noting that the amine-containing ETL can effectively reduce the work function of the metal cathode so that air stable metal such as Ag can be used as cathode, which is important for achieving stable OSCs.[32]

The effect of the ICL on the tandem cell performance was evaluated by choosing two different types of amine-containing polymers as the ETL, including the most commonly used polyfluorene-based ETL, poly[(9,9-bis(3′-(*N,N*-dimethylamino)-propyl)-2,7-fluorene)-*alt*-2,7-(9,9-dioctylfluorene)] (PFN),[43] and our newly designed PF3N-2TNDI, whose backbone is composed of the fluorene and naphthalene diimide (NDI) units conjugated by two thiophene spacers.[37,38] The new design was aimed to improve the electron mobility of the ETL as the NDI-based polymers are known to possess good electron transporting property. PFN is one the most successful ETLs used for cathode modification in both OSCs and organic light emitting diodes.[32,33] One of the key effects provided by PFN is the formation of desired interfacial dipole between the amine-functionalized side chains and the cathode electrode, which reduces the work function of the electrode and facilitates more efficient electron extraction in OSCs. The work functions of pure Ag film, Ag/PFN, and Ag/PF3N-2TNDI films measured by scanning Kelvin probe study were −4.5, −4.2, and −4.1 eV, respectively, suggesting that both ETLs could effectively improve the electron extraction property of the devices. However, it is also known that the device performance is very sensitive to the thickness of PFN and typically ultrathin (<5 nm) PFN is required to guarantee good performance in single-junction OSCs,[44] which may limit their use in tandem OSCs. To test the potential application of PFN in conventional tandem OSCs, devices with structure of ITO/PEDOT:PSS (40 nm)/sub-cell 1 (110 nm)/PFN(0–18 nm)/Ag (2 nm)/PEDOT:PSS(40 nm)/sub-cell 2(110 nm)/PFN (5 nm)/Ag (100 nm) were fabricated. In our first attempt to construct the tandem OSCs, the thicknesses of the front cell and back cell were based on the optimized conditions in their single-junction cells. An ultrathin Ag was also introduced in order to promote better charge recombinations at the ICL.[16,45,46] The thickness of PFN in our ICL varied from 4 to 18 nm. Theoretically, if efficient ICL was formed, the V_{oc} of tandem OSC should be equal to the sum of individual V_{oc} of the sub-cells, which is 1.67 V in our system.

The *J–V* curves of the tandem OSCs with PFN-based ICL are shown in **Figure 2**a and data are summarized in Table S2 of Supporting Information. Devices without any ETL in the ICL showed poor PCE with a low V_{oc} of 1.07 eV, which was attributed to the poor electron extraction contact of the front cell. In single-junction cells, the optimized thickness for PFN is ≈4 nm.[44,47] However, in the tandem OSCs, the introduction of a 4 nm PFN at the ICL only resulted in mediocre device performance with PCE of 6.41% and a V_{oc} of 1.34 V, which was far away from the optimized value. Further increasing the thickness of PFN did not improve the device performance; indeed, S-shaped *J–V* curves were observed. In the extreme case with thickness increasing to 18 nm, nearly no photocurrent can be produced from the devices. The trend observed here is very similar to that obtained in PFN-based single-junction devices owing to its poor electron transport property as the electron mobility (μ_e) of PFN measured using SCLC method was only 4.6×10^{-7} cm^2 V^{-1} s^{-1} (Figure S2 and Table S3 of Supporting Information). In

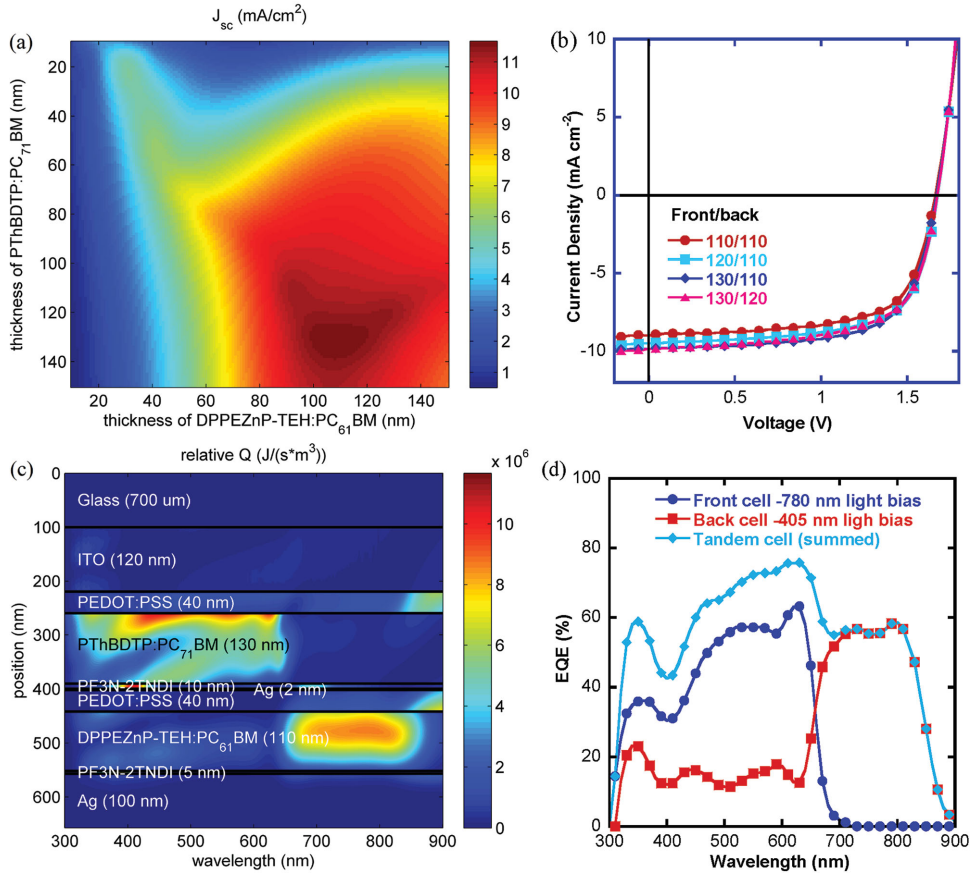

Figure 3. a) Simulated J_{sc} generated in conventional double-junction tandem OSC as a function of thickness of the front and back cells. b) *J–V* characteristics of double-junction tandem OSC with various thicknesses of front and back cells. c) The simulated energy distribution in the optimized tandem OSC with front cell of 130 nm and back cell of 110 nm. d) EQE spectra of the front cell, back cell, and summed EQE spectra of the front and back cells.

addition, when the thickness of PFN is <5 nm, electrons from the BHJ can tunnel through the PFN film and then collected by the cathode; however, when the thickness of PFN increases, it starts to behave as an electron blocking layer to PCBM due to its shallow lying LUMO (–2.4 eV), which resulted in a significant increase in resistance and forming of the S-shaped *J–V* curves.[44] To overcome this problem, the PFN in the ICL was replaced by the PF3N-2TNDI ETL with higher electron mobility of 2.5×10^{-4} cm^2 V^{-1} s^{-1} (Figure S2 and Table S3 of Supporting Information). The LUMO of PF3N-2TNDI (–3.9 eV) also matched well with that of PCBM, so even when the thickness of the ETL increases, electrons can still transport through the barrierless PCBM/PF3N-2TNDI interface. The *J–V* curves of the tandem devices are shown in Figure 2b. Tandem OSCs based on a 4 nm PF3N-2TNDI showed similar device property to the PFN one, with V_{oc} of only 1.32 V and PCE of 6.75%, suggesting that a very thin PFN or PF3N-2TNDI ETL film may not be able to provide a dense and uniform film to protect the bottom cell from being contacted with the HTL of the top cell. As a result, the HTL of the top cell may partially be in contact with the BHJ layer in the bottom cell and have resulted in an unfavorable contact for charge extraction, therefore leading to a decrease in V_{oc} of the tandem cell. However, when the thickness of P3FN-2TNDI further increased, an efficient ICL was formed with improved tandem cell characteristics. At a thickness of 9 nm, the V_{oc} of tandem OSCs increased to 1.67 V, which is the sum of the V_{oc}s of the individual sub-cells. The devices also showed a decent FF of 67% and J_{sc} of 8.99 mA cm^{-2}, leading to a PCE of 10.02%. In contrast to the PFN-based devices, further increasing the thickness of PF3N-2TNDI did not result in drastic decrease in performance. Even when the thickness of PF3N-2TNDI increased to 20 nm, the tandem OSCs still showed PCE up to 9.65%, which suggests that ETL with good charge transport property is important for constructing efficient ICL for high-performance tandem OSCs.

Although a reasonable PCE was obtained in our tandem OSCs, the thickness of each sub-cell had not yet been optimized and therefore there is still room for further improvement of the device performance. Optical modeling of the electric field distribution within the OSCs is a powerful means to predict the optimized structure for the complicated multilayer tandem devices.[10,13,22] Therefore, we performed optical analysis of our tandem OSCs using the transfer matrix modeling method to provide guideline on the best device architecture. The refractive index (*n*) and extinction coefficient (*k*) values of the different layers employed in our tandem OSCs are shown in the Supporting Information (Figure S3). According to the simulation result that is shown in **Figure 3**a, the optimal thicknesses of the front and back cell were 130 and 110 nm, respectively. To compare the simulated and experimental results, we linearly

Table 1. Device performances of conventional double-junction tandem solar cell with various thicknesses of front and back cells.

Thickness of front/back [nm]	J_{sc} [mA cm^{-2}]	V_{oc} [V]	FF [%]	PCE [%]
110/110	8.99	1.67	67	10.06
120/110	9.47	1.67	67	10.60
130/110	9.85	1.67	69	11.35
130/120	9.86	1.67	64	10.54

increased the thickness of the front cell from 110 to 130 nm while keeping the back-cell thickness to be 110 nm. Another attempt was to keep the thickness of front cell at 130 nm while increasing the thickness of back cell to 120 nm. It can be seen in Figure 3b and **Table 1** that when the thickness of the front cell increased from 110 to 130 nm, the V_{oc} and FF of tandem solar cell had no apparent change, but the J_{sc} of devices increased from 8.99 to 9.85 mA cm^{-2}, which resulted in a PCE of 11.35% at the optimal conditions. Increasing the back-cell thickness from 110 to 120 nm also resulted in a high J_{sc} of 9.86 mA cm^{-2}; however, there was a drop in FF from 69% to 64%, leading to a lower PCE of 10.54%. These experimental results matched very well with the simulation.

The simulated energy dissipation rate within the tandem OSC with a 130 nm front cell and a 110 nm back cell is shown in Figure 3c. The simulation showed that the energy distribution at the front cell is mainly localized at the wavelength range of 300–650 nm, while in the back cell only small portion of energy dissipated at that visible range but mainly localized in the infrared region of 650–900 nm. These simulated results can be compared with the EQE curves of the different sub-cells. To perform accurate EQE measurement for tandem OSCs, a high flux monochromatic light was selected to "turn on" one of the sub-cells, which eventually becomes a photoconductor and enables the measurement of EQE for the other sub-cell.[11] As shown in Figure 3d, the front cell absorbed most of the high-energy photons within the range of 300–650 nm and the maximum photoresponse reached 63.2% at 630 nm. The back cell showed a broad EQE spectrum with a relatively low EQE at the visible range and a high EQE at the infrared range, which is in good agreement with the simulated result. The J_{sc}s of the front cell and back cell obtained by integrating their EQE curves are 9.64 and 9.65 mA cm^{-2}, respectively, which are very consistent with the J_{sc} of the tandem OSC measured under AM 1.5 condition.

Since the intensity of the solar irradiation varies throughout the day, so it is useful to evaluate the performance of OSC under different illumination intensities. We therefore also studied the performance of our tandem cells under different incident illumination conditions and the results are shown in Figure S4 and Table S4 of Supporting Information. We observed that the PCE of the tandem cell continued to increase from 11.35% to 11.92% when the intensity decreased from 100 to 40–50 mW cm^{-2}. The improved performance at lower intensity is possibly due to the reduced bimolecular recombinations[48] and similar trend was also reported in both the single-junction[5] and tandem OSCs.[36] Further decreasing the light intensity led to a drop in PCE mainly due to the decrease in V_{oc}, but the PCE still remained larger than 10% before the light intensity decreased to less than 5 mW cm^{-2}. The high-performance achieved under a broad range of illuminated intensities further suggested that the tandem OSC can potentially be adopted to efficiently harvest sunlight under different conditions or even can be applied for indoor application by harvesting the room light.

Finally, the shelf-life stability of tandem OSCs was studied and flexible tandem devices were also demonstrated. In addition to the PCE, device stability is also an important parameter to evaluate the performance of OSCs. As discussed above, one of the most successful ICL structures is n-type metal oxides combined with PEDOT:PSS, e.g., ZnO/PEDOT:PSS; however, the stability of this junction is a major concern due to the acidic PEDOT:PSS-induced etching effect of ZnO.[31] In our ICL system, the metal oxide was replaced by PF3N-2TNDI and according to the chemical nature of the polymers, there are no obvious degradation pathways at the junction. Indeed, a small amount of acetic acid was added in the methanol solution of PF3N-2TNDI to improve its processibility, so it is unlikely the acidic PEDOT:PSS will degrade the PF3N-2TNDI. The result of PCE versus storage time is shown in **Figure 4**a; sample I was encapsulated with epoxy and stored in air with relative humidity of 60% at room temperature, while un-encapsulated sample II stored in nitrogen protected glove box as a comparison. In both cases, the PCE retained over 90% of their origin value after 30 d of storage, with PCE still higher than 10%. The result suggested that our ICL could be a potential choice for achieving tandem OSCs with long-term stability.

Another advantage of replacing the metal oxide with polymer ICL is its better mechanical flexibility, which is an important criterion for fabricating flexible devices. As shown in Figure 4b, flexible tandem OSCs were achieved by simply replacing the rigid glass/ITO substrates (sheet resistance of 12 Ω □$^{-1}$) with

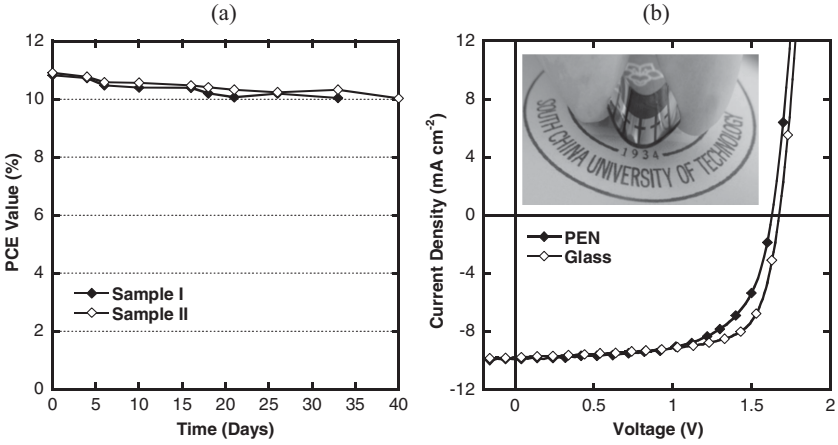

Figure 4. a) Device PCE versus storage time. Sample I: encapsulated with epoxy and stored in air with temperature at 25 °C and RH at 60%, sample II: stored in N_2 protected glove box without encapsulation. b) *J–V* characteristics of glass- and PEN-based tandem OSCs. Inset is the photograph of PEN-based flexible tandem OSC.

Table 2. Device performances of conventional tandem OSCs with glass and PEN as substrates.

Substrate	J_{sc} [mA cm^{-2}]	V_{oc} [V]	FF [%]	PCE [%]	Integrated J_{sc} [a)] [mA cm^{-2}]	Simulated J_{sc} [b)] [mA cm^{-2}]
Glass	9.85	1.67	69	11.35	9.64	11.66
(average)	9.83 ± 0.41	1.67 ± 0.01	67 ± 2.1	11.10 ± 0.16	–	–
PEN	9.89	1.63	63	10.16	–	–
(average)	9.86 ± 0.24	1.63 ± 0.01	61 ± 2.1	9.87 ± 0.29	–	–

[a)] Integrated J_{sc} from the EQE spectra; [b)] J_{sc} calculated by optical simulation where IQE was set as 100%. Statistic data achieved from 10 independent devices.

flexible PEN/ITO substrates (sheet resistance of 60 Ω □$^{-1}$) and the device performances are summarized in **Table 2**. Compared with glass-based OSCs, the PEN-based flexible devices exhibited a reduced PCE value due to the relatively large sheet resistance of the PEN/ITO substrates; however, the best performed device still reached a high PCE of 10.16%, further suggesting that our newly developed ICL is important for high-performance flexible tandem OSCs.

In summary, a new ICL configuration based on PF3N-2TNDI/Ag/PEDOT:PSS was developed and applied for the fabrication of high-performance tandem OSCs. Due to the presence of the polar amine groups for effective work-function modification and the relatively high mobility originated from the NDI-based polymer backbone, PF3N-2TNDI can form Ohmic contact with both sub-cells in the tandem OSCs and also protects the front cell from being destroyed by back-cell processing solutions. Tandem OSCs employing this ICL achieved a high PCE of 11.35% under 1 Sun condition and even reached ≈12% under 0.5 sun condition. Taking the advantage of the intrinsic flexibility of polymeric materials, we further applied our polymer-based ICL to fabricate flexible tandem OSCs with PCE over 10%, which is the best flexible OSCs reported. We believe that this new design of ICL can be generally applicable for other more efficient BHJ systems to eventually construct more efficient and printable tandem OSCs.

Experimental Section

Single-Junction OSC Fabrication: Indium tin oxide(ITO)-coated glass and PEN substrates were rinsed with standard procedure. Notice that the ultrasonic bath of PEN substrates was controlled within 5 min. The single-junction cells of the PThBDTP:PC_{71}BM and DPPEZnP-TEH:PC_{61}BM were fabricated according to previous reports[39,40] except that PF3N-2TNDI was used as the cathode interlayer and Ag (100 nm) was used as the cathode. In the case of DPPEZnP-TEH:PC_{61}BM, some samples were treated with solvent vapor by storing the samples in a chloroform-containing Petri dish for 30 s to complete the solvent annealing process. The PF3N-2TNDI was spin coated from MeOH solution to achieve a film of 5 nm.

Tandem OSC Fabrication: 40 nm PEDOT:PSS (Clevios P VP AI 4083) was spin coated onto ITO substrates and baked at 150 °C for 20 min. Then, PThBDTP:PC_{71}BM active layers (1:1.2 w/w) were spin coated from its mixed solvent of dichlorobenzene/1,8-diiodoctane (100:3 v/v) solution onto PEDOT:PSS to achieve films with thickness of 110–130 nm. The PFN or PF3N-2TNDI solution was spin coated onto PThBDTP:PC_{71}BM at a spin speed of 2000 rpm. By varying the concentrations from 0.5, 1, 2 to 4 mg mL^{-1}, the thickness of the resulted PFN and PF3N-2TNDI films were 4, 8, 12, 18 nm and 4, 9, 13, 20 nm, respectively. After that, a 2 nm ultrathin Ag was evaporated onto PFN or PF3N-2TNDI with a base pressure of 1×10^{-7} Torr. Subsequently, 40 nm PEDOT:PSS (Clevios P VP AI 4083) was spin coated onto the ultrathin Ag film in ambient atmosphere and baked at 100 °C for 10 min in a nitrogen protected glove box to remove the residual water. Then, 110–120 nm DPPEZnP-TEH:PC_{61}BM active layer was spin coated onto PEDOT:PSS from its mixed solvent of chlorobenzene/pyridine (100:1 v/v) solution and baked at 120 °C for 5 min to complete the thermal annealing process. The samples were then put into a chloroform contained Petri dish for 30 s to complete the solvent annealing process; after that, 5 nm PF3N-2TNDI was spin coated onto DPPEZnP-TEH:PC_{61}BM. Lastly, devices were finished by evaporating 100 nm Ag through a shadow mask in a vacuum chamber with a base pressure of 1×10^{-7} Torr.

Device Characterization: The *J–V* curves were measured on a computer-controlled Keithley 2400 sourcemeter under 1 sun, AM 1.5 G spectra from a class solar simulator (Taiwan, Enlitech); the light intensity was 100 mW cm^{-2} as calibrated by a China general certification center (CGC) certified reference monocrystal silicon cell (Enlitech). Before the *J–V* test, a physical mask of an aperture with precise area of 4 mm^2 was used to define the device area. The EQE study was performed on a commercial EQE measurement system (Taiwan, Enlitech, QE-R3011). Light biases of 470 and 780 nm were selected to excite the front and back sub-cells in the tandem devices.

Optical Modeling: The optical model was preformed based on the Transfer Matrix Formalism model. The optical parameters, *n* and *k*, of the different films were measured using a dual rotating-compensator Mueller matrix ellipsometer (ME-L ellipsometer, Wuhan Eoptics Technology Co., Wuhan, China). A more detailed description of the modeling and fitting methods for the optical parameters is provided in the Supporting Information.

Supporting Information

Supporting Information is available from the Wiley Online Library or from the author.

Acknowledgements

K.Z., K.G., and R.X. contributed equally to this work. The work was financially supported by the Ministry of Science and Technology of the People's Republic of China (No. 2014CB643500), the National Natural Science Foundation of China (No. 51521002, 51323003, 51573057, 21490573, and 21520102006) and Guangdong Natural Science Foundation (Grant No. S2012030006232). L.D. thanks National Natural Science Foundation of China (U1401244 and 21374025) for financial support.

Received: December 16, 2015
Revised: March 2, 2016
Published online: April 13, 2016

[1] G. Yu, J. Gao, J. C. Hummelen, F. Wudl, A. J. Heeger, *Science* **1995**, *270*, 1789.
[2] B. Kippelen, J.-L. Bredas, *Energy Environ. Sci.* **2009**, *2*, 251.

[3] L. Dou, J. You, Z. Hong, Z. Xu, G. Li, R. A. Street, Y. Yang, *Adv. Mater.* **2013**, *25*, 6642.
[4] Y. Liu, J. Zhao, Z. Li, C. Mu, W. Ma, H. Hu, K. Jiang, H. Lin, H. Ade, H. Yan, *Nat. Commun.* **2014**, *5*, 5293.
[5] Z. He, B. Xiao, F. Liu, H. Wu, Y. Yang, S. Xiao, C. Wang, T. P. Russell, Y. Cao, *Nat. Photonics* **2015**, *9*, 174.
[6] H. Hu, K. Jiang, G. Yang, J. Liu, Z. Li, H. Lin, Y. Liu, J. Zhao, J. Zhang, F. Huang, Y. Qu, W. Ma, H. Yan, *J. Am. Chem. Soc.* **2015**, *137*, 14149.
[7] V. Vohra, K. Kawashima, T. Kakara, T. Koganezawa, I. Osaka, K. Takimiya, H. Murata, *Nat. Photonics* **2015**, *9*, 403.
[8] X. Ouyang, R. Peng, L. Ai, X. Zhang, Z. Ge, *Nat. Photonics* **2015**, *9*, 520.
[9] Z. A. Page, Y. Liu, V. V. Duzhko, T. P. Russell, *Science* **2014**, *346*, 441.
[10] N.-K. Persson, O. Inganäs, *Sol. Energy Mater. Sol. Cells* **2006**, *90*, 3491.
[11] J. Y. Kim, K. Lee, N. E. Coates, D. Moses, T.-Q. Nguyen, M. Dante, A. J. Heeger, *Science* **2007**, *317*, 222.
[12] T. Ameri, N. Li, C. J. Brabec, *Energy Environ. Sci.* **2013**, *6*, 2390.
[13] A. R. b. M. Yusoff, D. Kim, H. Kim, F. K. Shneider, W. J. da Silva, J. Jang, *Energy Environ. Sci.* **2015**, *8*, 303.
[14] G. Dennler, M. C. Scharber, T. Ameri, P. Denk, K. Forberich, C. Waldauf, C. J. Brabec, *Adv. Mater.* **2008**, *20*, 579.
[15] F. Guo, N. Li, F. W. Fecher, N. Gasparini, C. O. R. Quiroz, C. Bronnbauer, Y. Hou, V. V. Radmilović, V. R. Radmilović, E. Spiecker, K. Forberich, C. J. Brabec, *Nat. Commun.* **2015**, *6*, 7730.
[16] A. Martinez-Otero, Q. Liu, P. Mantilla-Perez, M. M. Bajo, J. Martorell, *J. Mater. Chem. A* **2015**, *3*, 10681.
[17] J. Sakai, K. Kawano, T. Yamanari, T. Taima, Y. Yoshida, A. Fujii, M. Ozaki, *Sol. Energy Mater. Sol. Cells* **2010**, *94*, 376.
[18] D. W. Zhao, L. Ke, Y. Li, S. T. Tan, A. K. K. Kyaw, H. V. Demir, X. W. Sun, D. L. Carroll, G. Q. Lo, D. L. Kwong, *Sol. Energy Mater. Sol. Cells* **2011**, *95*, 921.
[19] S. Lu, X. Guan, X. Li, W. E. T. Sha, F. Xie, H. Liu, J. Wang, F. Huang, W. C. H. Choy, *Adv. Energy Mater.* **2015**, *5*, 1500631.
[20] L. Zuo, C.-Y. Chang, C.-C. Chueh, S. Zhang, H. Li, A. K. Y. Jen, H. Chen, *Energy Environ. Sci.* **2015**, *8*, 1712.
[21] C.-Y. Chang, L. Zuo, H.-L. Yip, Y. Li, C.-Z. Li, C.-S. Hsu, Y.-J. Cheng, H. Chen, A. K. Y. Jen, *Adv. Funct. Mater.* **2013**, *23*, 5084.
[22] C.-C. Chen, W.-H. Chang, K. Yoshimura, K. Ohya, J. You, J. Gao, Z. Hong, Y. Yang, *Adv. Mater.* **2014**, *26*, 5670.
[23] J. You, L. Dou, K. Yoshimura, T. Kato, K. Ohya, T. Moriarty, K. Emery, C.-C. Chen, J. Gao, G. Li, Y. Yang, *Nat. Commun.* **2013**, *4*, 1446.
[24] S. K. Hau, H.-L. Yip, K.-S. Chen, J. Zou, A. K.-Y. Jen, *Appl. Phys. Lett.* **2010**, *97*, 253307.
[25] C.-Y. Chang, L. Zuo, H.-L. Yip, C.-Z. Li, Y. Li, C.-S. Hsu, Y.-J. Cheng, H. Chen, A. K.-Y. Jen, *Adv. Energy Mater.* **2014**, *4*, 1301645.
[26] W. Li, A. Furlan, K. H. Hendriks, M. M. Wienk, R. A. J. Janssen, *J. Am. Chem. Soc.* **2013**, *135*, 5529.
[27] P. Boland, K. Lee, J. Dean, G. Namkoong, *Sol. Energy Mater. Sol. Cells* **2010**, *94*, 2170.
[28] S. Sista, M.-H. Park, Z. Hong, Y. Wu, J. Hou, W. L. Kwan, G. Li, Y. Yang, *Adv. Mater.* **2010**, *22*, 380.
[29] D. Lee, W. Ki Bae, I. Park, D. Y. Yoon, S. Lee, C. Lee, *Sol. Energy Mater. Sol. Cells* **2011**, *95*, 365.
[30] A. Puetz, F. Steiner, J. Mescher, M. Reinhard, N. Christ, D. Kutsarov, H. Kalt, U. Lemmer, A. Colsmann, *Org. Electron.* **2012**, *13*, 2696.
[31] J. Gilot, M. M. Wienk, R. A. J. Janssen, *Appl. Phys. Lett.* **2007**, *90*, 143512.
[32] F. Huang, H. Wu, Y. Cao, *Chem. Soc. Rev.* **2010**, *39*, 2500.
[33] C. Duan, K. Zhang, C. Zhong, F. Huang, Y. Cao, *Chem. Soc. Rev.* **2013**, *42*, 9071.
[34] Y. Zhou, C. Fuentes-Hernandez, J. W. Shim, T. M. Khan, B. Kippelen, *Energy Environ. Sci.* **2012**, *5*, 9827.
[35] A. R. b. M. Yusoff, S. J. Lee, H. P. Kim, F. K. Shneider, W. J. da Silva, J. Jang, *Adv. Funct. Mater.* **2014**, *24*, 2240.
[36] Y. Liu, C.-C. Chen, Z. Hong, J. Gao, Y. Yang, H. Zhou, L. Dou, G. Li, Y. Yang, *Sci. Rep.* **2013**, *3*, 3356.
[37] C. Sun, Z. Wu, H.-L. Yip, H. Zhang, X.-F Jiang, Q. Xue, Z. Hu, Y. Shen, M. Wang, F. Huang, Y. Cao, *Adv. Energy Mater.* **2015**, DOI: 10.1002/aenm.201501534.
[38] Z. Wu, C. Sun, S. Dong, X.-F. Jiang, S. Wu, H. Wu, H.-L. Yip, F. Huang, Y. Cao, *J. Am. Chem. Soc.* **2016**, *138*, 2004.
[39] J. Cao, L. Qian, F. Lu, J. Zhang, Y. Feng, X. Qiu, H.-L. Yip, L. Ding, *Chem. Commun.* **2015**, *51*, 11830.
[40] K. Gao, L. Li, T. Lai, L. Xiao, Y. Huang, F. Huang, J. Peng, Y. Cao, F. Liu, T. P. Russell, R. A. J. Janssen, X. Peng, *J. Am. Chem. Soc.* **2015**, *137*, 7282.
[41] A. Hadipour, B. de Boer, P. W. M. Blom, *Org. Electron.* **2008**, *9*, 617.
[42] S. Miller, G. Fanchini, Y.-Y. Lin, C. Li, C.-W. Chen, W.-F. Su, M. Chhowalla, *J. Mater. Chem.* **2008**, *18*, 306.
[43] F. Huang, H. Wu, D. Wang, W. Yang, Y. Cao, *Chem. Mater.* **2004**, *16*, 708.
[44] S. Liu, K. Zhang, J. Lu, J. Zhang, H.-L. Yip, F. Huang, Y. Cao, *J. Am. Chem. Soc.* **2013**, *135*, 15326.
[45] J. W. Shim, Y. Zhou, C. Fuentes-Hernandez, A. Dindar, Z. Guan, H. Cheun, A. Kahn, B. Kippelen, *Sol. Energy Mater. Sol. Cells* **2012**, *107*, 51.
[46] Z. Zheng, S. Zhang, M. Zhang, K. Zhang, L. Ye, Y. Chen, B. Yang, J. Hou, *Adv. Mater.* **2015**, *27*, 1189.
[47] K. Zhang, Z. Hu, R. Xu, X.-F. Jiang, H.-L. Yip, F. Huang, Y. Cao, *Adv. Mater.* **2015**, *27*, 3607.
[48] C.-Y. Chang, W.-K. Huang, Y.-C. Chang, K.-T. Lee, H.-Y. Siao, *Chem. Mater.* **2015**, *27*, 1869.

ADVANCED MATERIALS

Supporting Information

for *Adv. Mater.*, DOI: 10.1002/adma.201506270

High-Performance Polymer Tandem Solar Cells Employing a New n-Type Conjugated Polymer as an Interconnecting Layer

Kai Zhang, Ke Gao, Ruoxi Xia, Zhihong Wu, Chen Sun, Jiamin Cao, Liu Qian, Weiqi Li, Shiyuan Liu, Fei Huang, Xiaobin Peng,* Liming Ding,* Hin-Lap Yip,* and Yong Cao*

Supporting Information

High Performance Polymer Tandem Solar Cells Employing New n-type Conjugated Polymer as Interconnecting Layer

By Kai Zhang[1], Ke Gao[1], Ruoxi Xia[1], Zhihong, Wu[1], Chen Sun[1], Jiamin Cao[2], Liu Qian[2],Weiqi Li[3],Shiyuan Liu[3,4], Fei Huang[1], Xiaobin Peng[1]*,Liming Ding[2]*, Hin-Lap Yip[1]* and Yong Cao[1]*

[1] Institute of Polymer Optoelectronic Materials and Devices, State Key Laboratory of Luminescent Materials and Devices, South China University of Technology, Guangzhou 510640, P. R. China, E-mail: msfhuang@scut.edu.cn, chxbpeng@scut.edu.cn, msangusyip@scut.edu.cn,
[2] National Center for Nanoscience and Technology, Beijing 100190, P. R. China, E-mail: ding@nanoctr.cn
[3] State Key Laboratory of Digital Manufacturing Equipment and Technology, Huazhong University of Science and Technology, Wuhan, Hubei430074, P. R. China.
[4] Wuhan Eoptics Technology Co. Ltd., Wuhan, Hubei430075, P. R. China

n, k value measurement: At first, thin films with thickness of about 100nm are manufactured by depositing the studied materials on the ITO glass. Dual rotating-compensator Mueller matrix ellipsometer (ME-L ellipsometer, Wuhan Eoptics Technology Co., Wuhan, China)[1] was used to collect the ellipsometric data of the thin film samples. The layout of the MME in order of light propagation is PCr1SCr2A, where P and A stand for the polarizer and analyzer, Cr1 and Cr2 refer to the 1st and 2nd rotating compensators, and S stands for the sample. With this dual rotating-compensator configuration, the full Mueller matrix elements can be obtained in a single measurement. The spectral range is from 200nm to 1000 nm. The beam diameter can be changed from the normal value of about 3 mm to a value less than 200 μm with the focusing lens. The two arms of the instrument and the sample stage can be rotated to

change the incidence angle and azimuthal angle in the experiments. And then, the optical constant of the studied materials as well as the film thickness can be extracted from the measured ellipsometric data, by performing a weighted least-squares regression analysis method (Levenberg-Marquardt algorithm)[2]. In the data analysis, the optical constant of the ITO film as well as the glass are determined by performing a measurement on a blank ITO coated film. And the optical constant of the studied materials can be characterized by superimposing the general oscillator models (such as Lorentz model,[3]Tauc-Lorentz model,[4] Gaussian model[5] etc.), which can characterize simple materials. This is done by linearly adding the general oscillator models to the polo model, which is a zero-broadening oscillator.

In our experiment, in order to achieve a high accuracy result, the incident angle is set to be 55° to 65° by 5° to eliminate the effect of data coupling. The spectral range is 300 nm to 1000 nm by 1nm. Figure S2 a and b show the measured optical constant of the studied materials.

Optical modeling: In the series structure, voltage is the sum of each sub cell but current is limited by the minimum one of all sub-cells in theory. To deal with this ‘‘Cask Effect’’ of short circuit current density (J_{sc}), thicknesses of the BHJ layers should be optimized in order to achieve a balanced and high J_{sc}. The optical model based on Transfer Matrix Formalism (TMF) can simplify the optimization design and predict the performance of device with certain structure.

The TMF method analyzes the propagation of light incident on stacks of layers. This theory assumes that all layers are homogeneous and their interfaces are flat and parallel so that each layer can just be described by its thickness and optical parameter N which is so-called

complex refractive index and all of these parameters can be determined by spectroscopic ellipsometry. In addition, the incidence light should be described by plane waves. Based on these aforementioned assumptions, light propagation in medium or at interface can be skillfully described by matrices due to the linearity and continuity of electric field component. TMF takes account of the effects of light wave character and reflection and transmission at medium interfaces so it can give a precise description of light propagation in layer stacks.

Optical model can utilize TMF to calculate the optical electric field intensity (|E|) at each position of the whole multilayer structure. Then we can use the relationship between |E| and absorption strength to obtain the distribution of energy. After integrating the absorbed energy in each BHJ layer, we can get J_{sc} of each sub-cell and the smallest one represents the whole device's J_{sc}. Because the model just considers the optics aspect, the J_{sc} is an ideal value based on the 100-percent IQE, that is, all absorbed photons are contributing to the steady state photocurrent.

We can get J_{sc}s of devices with different thicknesses of BHJ layers by optical model and then easily find the optimal design.

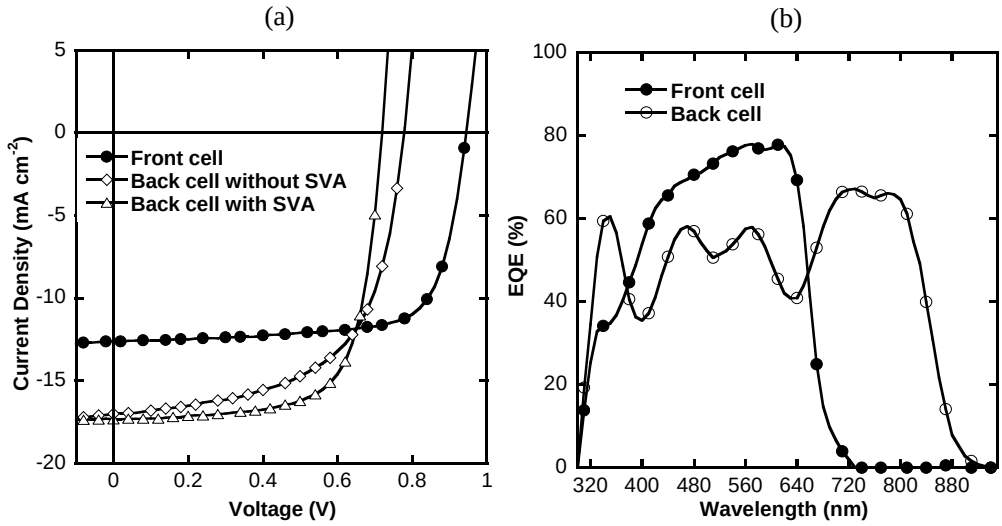

Figure S1. a) *J-V* characteristics of single junction front cell and single junction back cell w/o SVA. b) EQE spectra of single junction front cell and single junction back cell.

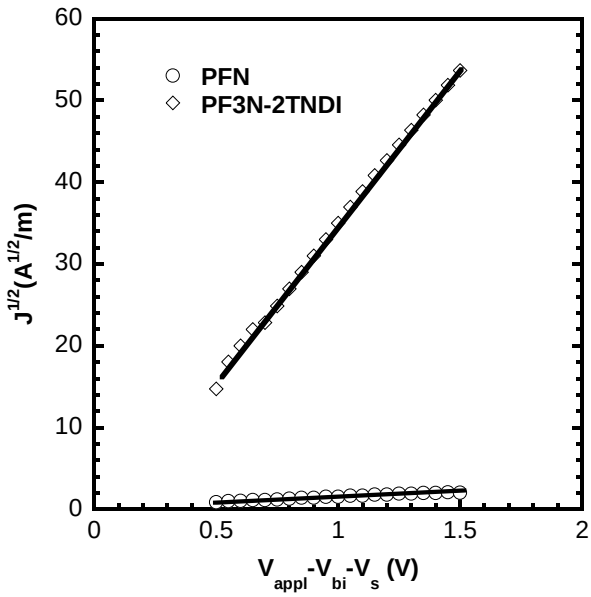

Figure S2. $J^{1/2}$~V characteristics of electron-only devices with device configuration: ITO/Al/PFN or PF3N-2TNDI (100 nm)/Al.

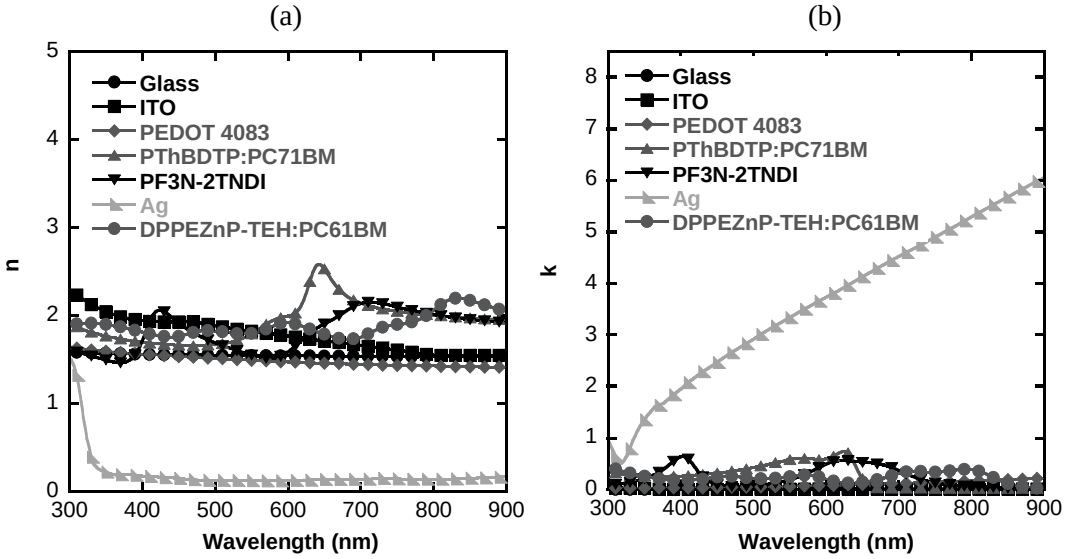

Figure S3. a) Refraction index (n) and b) extinction coefficient (k) values of all the different layers employed in tandem OSCs.

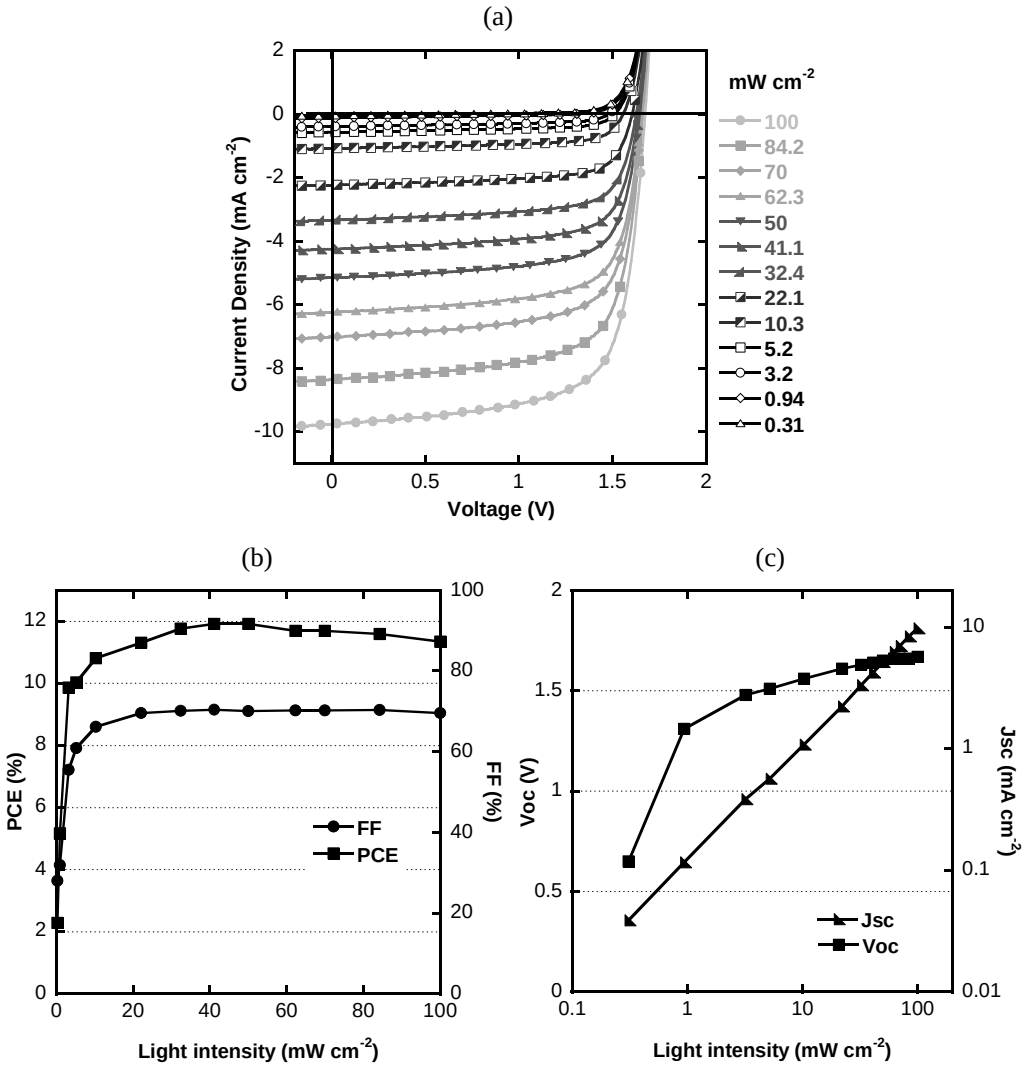

Figure S4. a) *J-V* characteristics of optimized tandem solar cell tested under different light intensity conditions. b) PCE value and FF versus light intensity. c) V_{oc} and J_{sc} versus light intensity

Table S1. Device performances of single junction front cell and single junction back cell w/o SVA.

Single junction cell	SVA	Integrated J_{sc} (mA cm^{-2})	Measured J_{sc}(mA cm^{-2})	V_{oc} (V)	FF (%)	PCE (%)
Front cell	\	12.70	12.60	0.95	74	8.86
Back cell	without	\	17.01	0.78	61	8.09
Back cell	with	17.06	17.32	0.72	70	8.73

Table S2. Device performances of conventional tandem solar cells employing ICL constructed with different thickness PFN and PF3N-2TNDI. The thickness of front/back cell is 110/110 nm

ETL in ICL	Thickness (nm)	J_{sc} (mA cm^{-2})	V_{oc} (V)	FF (%)	PCE (%)	Rs
None	0	8.22	1.02	54	4.54	897
PFN	4	8.57	1.34	56	6.41	1105
	8	7.63	1.46	27	3.05	9293
	12	4.80	1.31	19	1.17	15159
	18	0.249	1.09	22	0.06	142139
PF3N-2TNDI	4	8.46	1.32	61	6.75	806
	9	8.99	1.67	67	10.02	634
	13	9.00	1.65	68	10.06	634
	20	8.55	1.65	68	9.65	622

Table S3. The energy level and mobility of PFN and PF3N-2TNDI together with the work function of bare Ag and PFN, PF3N-2TNDI coated Ag.

	LUMO (eV)	HOMO (eV)	Mobility ($cm^2 V^{-1} \cdot s^{-1}$)	Work function (eV)
PFN	-5.61	-2.41	4.6×10^{-7}	\
PF3N-2TNDI	-5.55	-3.91	2.5×10^{-4}	\
Ag/PFN	\	\	\	-4.2
Ag/PF3N-2TNDI	\	\	\	-4.1
Ag	\	\	\	-4.5

Table S4. Device performances of optimized tandem solar cell tested under different light intensity conditions, as obtained from standard AM 1.5G (100 mW cm^{-2}) illumination using a set of neutral optical filters.

Light intensity (mW cm^{-2})	J_{sc} (mA cm^{-2})	V_{oc} (V)	FF (%)	PCE (%)
100	9.85	1.67	69	11.35
84.1	8.36	1.66	70	11.60
70	7.02	1.66	70	11.69
62.3	6.24	1.66	70	11.69
50	5.15	1.65	70	11.92
41.1	4.24	1.64	70	11.92
32.4	3.33	1.63	70	11.76
22.1	2.23	1.61	69	11.21
10.3	1.08	1.56	66	10.82
5.2	0.57	1.51	61	10.03
3.2	0.38	1.48	55	9.87
0.94	0.12	1.31	32	5.18
0.31	0.04	0.65	28	2.29

Reference:

1. S. Liu, X. Chen, C. Zhang, Development of a broadband Mueller matrix ellipsometer as a powerful tool for nanostructure metrology, Thin Solid Films 584 (2015) 176-185
2. W. H. Press, S. A. Teukolsky, W. T. Vetterling, and B. P. Flannery, Numerical Recipes: The Art of Scientific Computing, 3rd ed. (Cambridge University Press, Cambridge, 2007)
3. H. Fujiwara, Spectroscopic Ellipsometry: Principles and Applications (John Wiley & Sons, 2007).
4. Jellison GE, Jr., Modine FA. Parameterization of the optical functions of amorphous materials in the interband region. Applied Physics Letters, 69(3) (1996) 371 -373.
5. Tiwald TE, Thompson DW, Woollam JA, Paulson W, Hance R. Application of IR variable angle spectroscopic ellipsometry to the determination of free carrier concentration depth profiles. Thin Solid Films. 313(2) (1998) 661–666.